An Explicit Minimum-Loss Control Strategy for Dual VSI DFIG-dc Systems

Gil D. Marques, *Senior Member, IEEE,* Matteo F. Iacchetti, *Senior Member, IEEE,*
and Sérgio M. A. Cruz *Senior Member, IEEE*

***Abstract*—This paper presents a new minimum-loss control strategy for vector-controlled dual-VSI DFIG-dc systems. The optimization is based on a simplified formalism using Lagrange multipliers to determine the optimal stator frequency, stator/rotor magnetizing current split, and the magnetizing flux magnitude as a function of the machine operating conditions, namely speed and torque. Compared with existing minimum-loss control schemes, the proposed approach provides an explicit solution for all the three optimal quantities, which makes the implementation and control design easier, thus avoiding the use of an additional proportional-integral controller to solve the flux implicit optimality condition. The theoretical framework also includes a sensitivity analysis against DFIG parameter variations, to appraise the robustness of the proposed control scheme. The devised approach and related control implementation scheme are validated with simulation and experimental results.**

***Index Terms*— Dc power system, DFIG, Dual-VSI DFIG, Efficiency improvement, Field-weakening, Minimum loss control.**

NOMENCLATURE

General

E	Electromotive force
i	Steady state current (p.u.).
$\boldsymbol{I_{md}}$	Magnetizing current (p.u.).
$\boldsymbol{I_{mq}}$	Core loss representing current (p.u.).
$\boldsymbol{L_s, L_m}$	Stator and mutual inductance (p.u.).
$\boldsymbol{L_{ks}, L_{kr}}$	Stator, rotor leakage inductance (p.u.).
$\boldsymbol{P_{se0}},\ \boldsymbol{P_{re0}}$	Stator/rotor eddy current losses at standstill (p.u.).
$\boldsymbol{P_{sh0}},\ \boldsymbol{P_{rh0}}$	Stator/rotor hysteresis power losses at standstill (p.u.).
$\boldsymbol{r_s, r_r}$	Stator and rotor resistances (p.u.).
$\boldsymbol{T_D}$	Electromagnetic torque (p.u.).
u	Voltage (p.u.).
U	Voltage.
$\boldsymbol{\lambda}$	Lagrange multiplier.
$\boldsymbol{\psi}$	Flux linkage (p.u.).
$\boldsymbol{\psi_m}$	Airgap flux linkage (p.u.).
$\boldsymbol{\omega_b}$	Base frequency (rad/s).
$\boldsymbol{\omega_m}$	Rotor speed (p.u.).
$\boldsymbol{\omega_s, \omega_r}$	Stator and rotor frequencies.

Superscripts

*	Reference value.
op	Relative to optimal point of operation.

Subscripts

d, q	Variables on the airgap flux reference frame.
s, r	Stator/ rotor.
N	Rated value.

I. INTRODUCTION

The classical ac doubly-fed induction generator (DFIG), interfaced with the mains, has been widely used in wind energy conversion systems and other variable-speed power generation applications [1]-[2], using cheaper de-rated power converters without sacrificing full controllability.

In wind farms, when dc is used for interconnecting several DFIG systems [3]-[6], the DFIG-dc version is a possible choice because it simplifies the overall system. The implementation of a dual voltage source inverter (VSI) can help improve torque smoothness and power quality, as described in [7]. As shown in Fig. 1, this system comprises a wound rotor induction machine (WRIM) fed through the stator and rotor windings by two VSI converters connected to a shared dc-link.

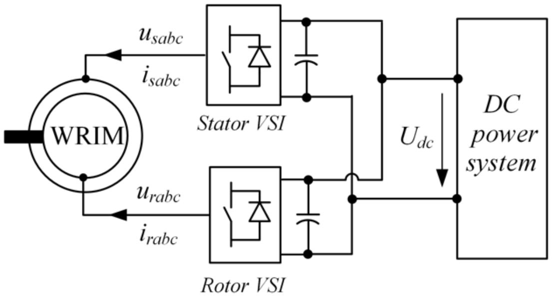

Fig. 1 Layout of a dual-VSI DFIG-dc system.

Initially, dual-VSI WRIMs were proposed for high-power motor drives [7]-[9], with a shared dc-link supplied by a third VSI connected to the AC mains and functioning as an active rectifier. One of the first applications of the dual-VSI layout to DFIG-dc drives was suggested in [6], where the DFIG is

Manuscript received Month xx, 2xxx; revised Month xx, xxxx; accepted Month x, xxxx. This work was supported by national funds through Fundação para a Ciência e a Tecnologia (FCT), with references UIDB/50021/2020, UIDB/EEA/50008/2020 and UID/CEC/50021/2013.

G. D. Marques is with the INESC-ID, Instituto Superior Técnico (IST), Universidade de Lisboa, Av. Rovisco Pais, no 1, 1049-001 Lisbon, Portugal (e-mail: gil.marques@tecnico.ulisboa.pt).

M. F. Iacchetti is with the Department of Energy of Politecnico di Milano, via Lambruschini 4, Milan, Italy, and with the School of Electrical and Electronic Engineering, The University of Manchester, Manchester, M13 9PL, U.K. (e-mail: matteo.iacchetti@poloimi.it).

S. M. A. Cruz is with the University of Coimbra, Department of Electrical and Computer Engineering, and with Instituto de Telecomunicações, Polo 2 - Pinhal de Marrocos, P-3030-290 Coimbra, Portugal, (e-mail: smacruz@ieee.org).

operated at a *slip* = -1 to achieve equal stator/rotor active power sharing. The solution in [6] adopts a vector control strategy based on the magnetizing flux linkage, while rotor-flux and stator-flux vector control schemes for the dual-VSI DFIG-dc system were proposed in [3] and [8], respectively.

Optimizing efficiency, and thus reducing losses, is becoming an important concern in power generation drives. In the classic ac DFIG system, the stator/rotor magnetizing current, and the stator / grid-side-converter (GSC) reactive power splits can be optimized to minimize losses [13] - [16]. Reference [14] presents a thorough analysis of the dual-VSI WRIM operating modes and constraints, and their impact on copper loss minimization.

In DFIG-dc systems the stator frequency or slip are free variables which can serve as a further degree of freedom for total loss minimization. In [17]-[18], minimum-loss control has been formulated for a single VSI DFIG-dc system. Copper loss minimization in a dual-VSI DFIG-dc drive was explored in [8] with a predictive control scheme which, however, maintains the stator frequency at the WRIM rated value, then causing a significant variation in core losses.

Further study on loss optimization was carried out in [19], proposing a comprehensive minimum-loss control strategy that considers copper, core, and semiconductor losses. This strategy is based on Lagrange multipliers, leading to three simple rules to enforce minimum loss conditions. Real-time implementation details, including optimal frequency, magnetizing flux, and magnetizing current split reference generation and inner flux were also discussed, while a stability study considering only inner control loops was presented in [20]. As a main drawback, the method in [19] only provides an implicit optimality condition for the magnetizing flux magnitude. This must be solved in real-time by using an additional proportional-integral (PI) controller, with no easy tuning, more complex implementation, and non-trivial stability properties [20]. Furthermore, the optimization accuracy against parameter variations was not addressed in previous work.

Compared to previous work on the subject – and in particular [19], this paper includes the following key innovations:

- Provision of a simplified mathematical model allowing the derivation of *fully analytic* optimality conditions.
- New and explicit formulation for the optimal flux level as a function of the reference torque and speed – this then serves as a direct input reference for the flux controller.
- Discussion of the physical meaning of Lagrange multipliers beyond their role of mere slack optimisation variables – with the first Lagrange multiplier being identified as the variable conjugate of torque to determine the total losses, which eases the sensitivity analysis against parameter variations.
- Thorough optimal-loss sensitivity analysis against WRIM parameter variation to justify the validity of the proposed solution.

The paper is structured as follows. Section II gives a brief description of the method presented in [19] and the most relevant results. It will be shown that there are four optimal operating zones. A simplified optimization procedure using Lagrange multipliers is presented in Section III. This section derives some key analytic results which form the basis for the synthesis of the new control method shown in Section V. Section IV presents a comprehensive discussion of the analytic relationships defining the optimal control variables, including a detailed comparison against results obtained with a numeric optimization method. Section V introduces the new control scheme based on the analytic optimization presented in previous Sections. A sensitivity analysis to WRIM parameters mismatches is conducted in Section VI to assess the robustness of the control method. Section VII presents some experimental results, and the conclusions are drawn in Section VIII.

II. MODELLING BACKGROUND

A. Equivalent Circuit

The system is mathematically described using the equivalent circuit shown in Fig. 2, with p.u. variables.

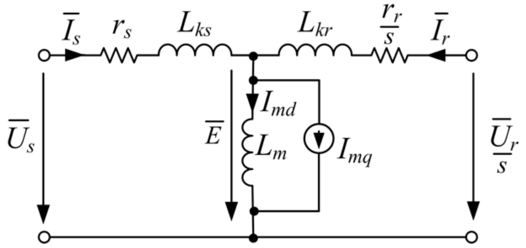

Fig. 2 Equivalent circuit of the induction machine.

Core losses are represented by the I_{mq} current source, and copper losses, in the stator and rotor, by resistances r_s and r_r, respectively. Per unit values are used throughout this paper. Motor convention is adopted for all electric quantities (positive when feeding the machine) and generator convention is used at the shaft.

B. Phasor Diagram Near an Optimal Operating Point

In [19] it was shown that the optimal operating points for the dual-VSI DFIG-dc system have slip values that are close to -1. By utilizing airgap flux orientation in both the study and control system, the phasor diagram shown in Fig. 3 is obtained.

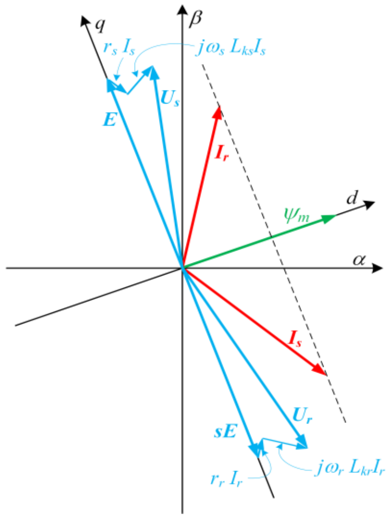

Fig. 3 Steady-state phasor diagram for negative slip ($s = -1$), with the generator running close to the minimum loss operating point [19].

The stator and rotor voltages are in opposite quadrants of the *dq* reference frame. Other control systems rather than airgap orientation can be used, but this latter option leads to compact expressions for core, Joule loss and optimal variables.

C. Optimization Conditions and Control Regions

Fig. 4 presents the optimal airgap flux surface according to [19], and shows that there are four different operating regions:

A – Minimum flux region: for small torque levels, when the flux hits the minimum value, here set at 0.5 *p.u*.

B – Low torque region: the optimization of the flux level aims to minimize core losses while no constraints are active; in this region, the optimal flux level is strongly dependent on torque and only weakly dependent on speed.

C – Maximum flux region: for high torque levels and low or medium speeds – the flux reaches the maximum value of 1 p.u. In practice, a smaller value is used.

D – Maximum voltage region: voltage constraint active. This corresponds to the classic field-weakening region.

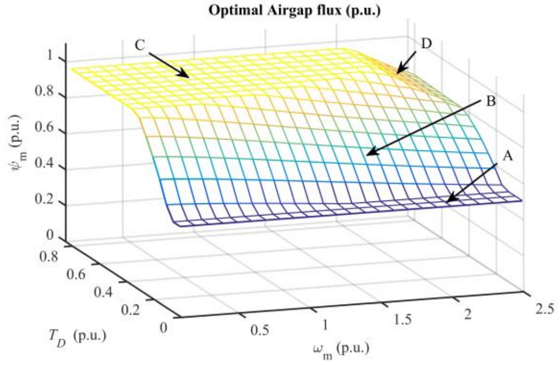

Fig. 4 Airgap flux in the four operating regions.

The minimum-loss control strategy presented in [19] uses airgap flux control and implements three conditions:

1) *Optimal frequency condition*. This is the same in regions A, B, C, Fig. 4, and it is slightly modified in region D. The stator and rotor frequencies depend on the rotor speed and on the WRIM parameters.
2) *Optimal magnetizing current split condition*. It requires stator and rotor resistive voltage drops due to the *d*-axis current components to be equal.
3) *Optimal flux condition*. This is only relevant in region B [19]. If semiconductor losses are neglected, this relation is translated into the equality of the *d*- and *q*-axis component losses.

III. OPTIMIZATION VIA LAGRANGE MULTIPLIERS

This section briefly presents a simplified mathematical formalism for the dual VSI DFIG-dc optimization. Unlike in [19], for better understanding and to derive explicit conditions, only core and Joule losses are considered, neglecting semiconductor loss component proportional to current – while the loss proportional to I^2 can be easily represented with “increased” WRIM resistance values. This assumption is acceptable also considering the new generation of power electronic devices, like silicon carbide and gallium nitride, which allow higher efficiency in the power electronics conversion [21]-[25] and make semiconductor losses much smaller than WRIM losses.

The study presented in this paper is relevant to regions A, B and C only, being the voltage constraint active in region D.

A. Lagrange Multipliers Formalism

In the analytic optimization, current I_{mq} (see Fig. 2) is neglected for current calculation purpose because, as it will be seen later on, it is much smaller than the torque-producing current I_{rq} (see Fig. 5). This leads to:

$$i_{sq} = -i_{rq}. \tag{1}$$

Equation (1) allows eliminating i_{sq}, by choosing i_{rq} as an independent state variable in the model.

The Lagrange function used here, neglecting winding eddy-losses, is therefore:

$$W_L = \begin{Bmatrix} \psi_m^2 f(\omega_s,\omega_r) + r_s\left(i_{sd}^2 + i_{rq}^2\right) + r_r\left(i_{rd}^2 + i_{rq}^2\right) \\ -\lambda_1\left(\psi_m i_{rq} - T_D\right) \\ -\lambda_2\left(L_m\left(i_{sd} + i_{rd}\right) - \psi_m\right) \end{Bmatrix}, \tag{2}$$

with the auxiliary function $f(\omega_s,\omega_r)$ defined as:

$$f(\omega_s,\omega_r) = P_{sh0}\omega_s + P_{rh0}\omega_r + P_{se0}\omega_s^2 + P_{re0}\,\omega_r^2. \tag{3}$$

Since (1) is adopted, (2) uses only two Lagrange multipliers, in contrast to [19].

The flux constraint can play two different roles. In region B, the flux is treated as an optimization variable, whereas in regions A and C, where the flux is subject to a minimum/maximum constraint, it is treated as a parameter.

Because minimum-loss operation is achieved at negative slips, the rotor frequency in this paper is defined as $\omega_r = \omega_m - \omega_s$. Since ω_m is an input, ω_s is the only “free” frequency to be determined by the optimization process.

Optimal points are achieved when the gradient of W_L is zero. The partial derivatives of (2) with respect to the stator and to the rotor current components are:

$$\frac{\partial W_L}{\partial i_{sd}} = 2r_s i_{sd}^{op} - \lambda_2^{op} L_m = 0 \tag{4}$$

$$\frac{\partial W_L}{\partial i_{rd}} = 2r_r i_{rd}^{op} - \lambda_2^{op} L_m = 0 \tag{5}$$

$$\frac{\partial W_L}{\partial i_{rq}} = 2(r_s + r_r) i_{rq}^{op} - \lambda_1^{op}\psi_m^{op} = 0. \tag{6}$$

Taking the derivative of (2) with respect to the Lagrange multipliers yields:

$$T_D = \psi_m^{op}\, i_{rq}^{op} \tag{7}$$

$$\psi_m^{op} = L_m\left(i_{sd}^{op} + i_{rd}^{op}\right). \tag{8}$$

The derivative of (2) with respect to the airgap flux gives:

$$2\,\psi_m^{op} f(\omega_s,\omega_r) - \lambda_1^{op}\, i_{rq}^{op} + \lambda_2^{op} = 0. \tag{9}$$

The derivative of (2) with respect to stator frequency ω_s is:

$$\frac{\partial W_L}{\partial \omega_s} = \psi_m^2\,\frac{\partial f(\omega_s,\omega_r)}{\partial \omega_s} = 0. \tag{10}$$

B. Optimal Stator Frequency Condition

Considering (10), (3), and $\omega_r = \omega_m - \omega_s$ and solving for ω_s yields:

$$\omega_s^{op} = \frac{P_{rh0}-P_{sh0}}{2(P_{se0}+P_{re0})} + \frac{P_{re0}}{(P_{se0}+P_{re0})}\,\omega_m. \tag{11}$$

Expression (11) determines the first optimal condition setting the stator frequency ω_s^{op} and consequently the rotor frequency ω_r^{op} as a function of ω_m. This condition does not depend on the flux and current levels and is valid also when the maximum flux level is used [19]. Thus, the optimal stator and rotor frequencies are functions of the rotor speed ω_m. The auxiliary function to represent core losses is a function of the rotor speed $f(\omega_m)$. If $P_{sh0} = P_{rh0}$ and $P_{se0} = P_{re0}$ results in a constant slip of -1.

C. Optimal d-axis Current Split Condition

Combining (4) and (5) produces the second optimal condition called "*magnetizing current split*" condition [19]:

$$r_r i_{rd}^{op} = r_s i_{sd}^{op}. \tag{12}$$

D. Optimal Flux Condition

Using (5), (6), (8), (9) and (12) it is possible to obtain the condition for the optimal flux, which is:

$$\underbrace{\psi_m^{op^2} f(\omega_m) + r_s i_{sd}^{op^2} + r_r i_{rd}^{op^2}}_{p_{d-axis}} = \underbrace{(r_s + r_r) i_{rq}^{op^2}}_{p_{q-axis}}. \tag{13}$$

This requires the d-axis component losses p_{d-axis} to equal the q-axis component losses p_{q-axis}. The total losses p_t is the sum of $p_{d-axis} + p_{q-axis}$. A generalization of (13), accounting for all converter losses, was formulated in [19].

IV. OPTIMAL RESULTS AND INTERPRETATION

A. Analytic Solution for the Optimal State Variables

The optimal values of i_{sd}, i_{rd}, i_{rq}, ψ_m, λ_1, and λ_2 come from the solution of the non-linear system comprising (5)-(8) and (12)-(13). Solving (12) for i_{sd} enables its elimination in (8) and (13). Equations (8) and (7) can then be solved for i_{rd} and i_{rq} as a function of ψ_m:

$$i_{rd} = \frac{\psi_m}{L_m(1+r_r/r_s)} \qquad , \qquad i_{rq} = T_D/\psi_m. \tag{14}$$

Replacing (14) into (13) yields an equation with ψ_m as the only unknown:

$$\left(f(\omega_m) + \frac{r_s r_r}{L_m^2(r_s+r_r)}\right)\psi_m^2 - (r_s + r_r)\,\frac{T_D^2}{\psi_m^2} = 0. \tag{15}$$

Solving (15) gives the optimal ψ_m as a function of the input torque reference and speed for the operating region B:

$$\psi_m^{op} = \sqrt[4]{\frac{L_m^2(r_s+r_r)^2}{f(\omega_m)L_m^2(r_s+r_r)+r_s r_r}}\,\sqrt{T_D}. \tag{16}$$

Replacing (16) into (14), (5) and (6), provides optimal values for the remaining state variables and Lagrange multipliers. In particular, i_{sd}, i_{rd}, i_{rq}, and λ_2 (not reported here for the sake of simplicity) exhibit a "$\sqrt{T_D}$-like" trend versus torque, while λ_1 is constant in region B

$$\lambda_1^{op} = 2\sqrt{f(\omega_m)\,(r_s + r_r) + \frac{r_s r_r}{L_m^2}}. \tag{17}$$

In Regions A and C, (16) is replaced by the constant minimum and maximum flux limits, so that i_{sd} and i_{rd} become constant and so does λ_2 via (5), while λ_1 becomes proportional to torque via (6) and (7).

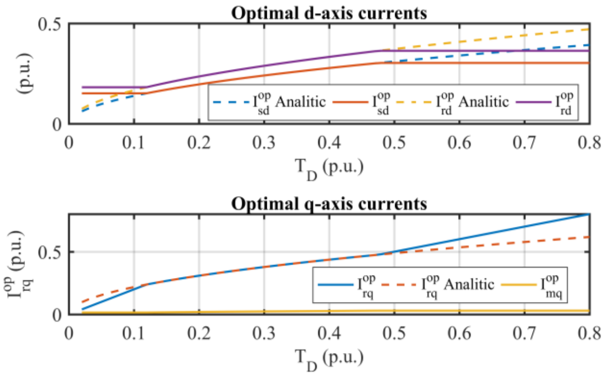

Fig. 5 Optimal currents ($\omega_m = 1\,p.u.$).

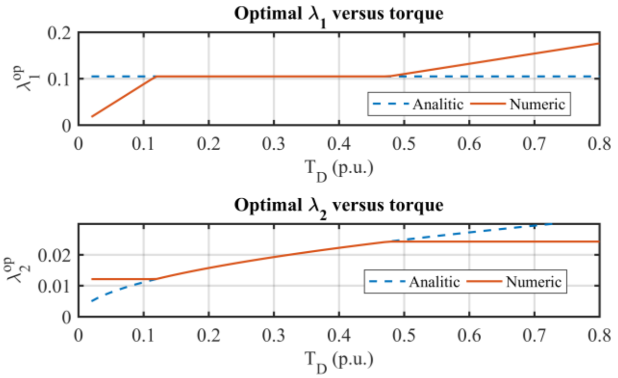

Fig. 6 Optimal Lagrange multipliers ($\omega_m = 1\,p.u.$): numeric optimization in the whole operating range and analytic solution in Region B.

B. Discussion

For preliminary validation and discussion, Fig. 5 to Fig. 7 compare the analytic solution for the optimal state variables at ω_m =1 p.u. with the numeric optimization results based on a full formulation of total losses including the effect of i_{mq} on torque (see Fig. 2).

Fig. 5 shows the numeric optimal currents versus torque over operating regions A (low torque), B, and C (high torque) along with the analytic values in region B. With the considered system parameters, region B stretches from $T_D \approx 0.1$ p.u. up to $T_D \approx 0.5$ p.u.

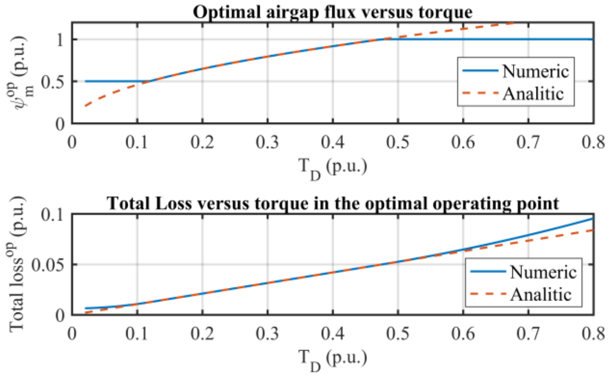

Fig. 7 Optimal flux and losses ($\omega_m = 1\ p.u.$): numeric optimization in the whole operating range and analytic solution in Region B.

The i_{sd} - i_{rd} split set by (12) it is clearly visible. For minimum and maximum flux levels, the d-axis current components are constant, and the q-axis currents are proportional to torque, (7). The complete loss formulation indicates that the I_{mq} current is much smaller than I_{rq}, hence justifying its suppression in formulation (2) and the subsequent analytic solution (16)-(17). In region B, the aforementioned "$\sqrt{T_D}$-trend" is clearly visible in all optimal variables except for λ_1. The constant trend of λ_1, as predicted by (17), is also confirmed.

In regions A and C, the derivative of λ_1^{op} with respect to torque is inversely proportional to $1/\psi_m^2$, according to (6) and (7), so the slope of λ_1^{op} in region A is higher than in region C.

Replacing the expressions of the optimal variables $\mathbf{x}^{op}(T_D)$ (i.e. (15)-(16) etc.) for Region B into the Lagrange function W_L (2) gives the optimal total losses $P_{total}^{op}(T_D)$ as a function of torque. After some manipulations, it can be proven that the derivative of $P_{total}^{op}(T_D)$ with respect to T_D is equal to the Lagrange multiplier λ_1^{op}

$$\frac{dP_{total}^{op}}{dT_D} = \frac{\partial W_L^{op}}{\partial T_D} = \lambda_1^{op}. \tag{18}$$

This is valid for regions A, B and C. The Lagrange multiplier λ_1^{op} is known as the shadow price. In region B only, λ_1^{op} does not depend on torque, and it can be verified that:

$$P_{total}^{op} = \lambda_1^{op}\, T_D. \tag{19}$$

This can also be observed in Fig. 7 where the optimal flux and losses are presented. In region B, λ_1^{op} (17) is independent of torque, and the total losses are proportional to the drive torque via λ_1^{opt}. The flux level is adjusted to minimize total losses. In this case, the only inputs to the system are the torque T_D and rotor speed ω_m. Clearly, when the flux constraints become active (i.e. in regions A and C), both in the minimum and maximum flux regions, losses are greater than the optimal value in (19), as shown in Fig. 7.

In regions A and C, the flux is limited, and its limit value is an input rather an optimization variable. At the optimal point, the losses are dependent on the limit flux value adopted. After some similar calculation that led to (18), results in:

$$\frac{dP_{total}^{op}}{d\psi_m} = 2\psi_m f(\omega_s, \omega_m) - \lambda_1^{op} I_{rq}^{op} + \lambda_2^{op}\,. \tag{20}$$

This determines how the total losses vary in regions A and C with respect to the adopted limit flux. The results are presented in Fig. 8.

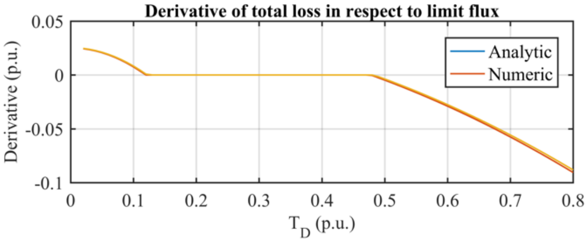

Fig. 8 Derivative of the total loss with respect to the flux limit. The analytic result was obtained using (20).

The analytic result refers to (20). In region A, an increase of the limit flux results in an increment of losses. Conversely, in region C, increasing the limit flux results in a loss reduction.

C. Influence of the Rotor Speed

The rotor speed impacts the total losses in two ways:

- via core losses, which increase with frequency.
- by determining the torque value at which the flux constraints are triggered, and the system enters regions A or C, then causing sub-optimal losses.

In region B, due to the monotonic trend of $f(\omega_m)$, (16) shows that the optimal flux at a given torque decreases when speed increases. Consequently, at high speeds, the system will start using the maximum flux for higher torque values then enlarging region B where the optimal losses are at minimum. Conversely, in regions A and C the flux is limited, and the state variables do not depend on speed. Nonetheless, total losses will increase with speed due to an increase in both stator and rotor frequencies.

V. NEW CONTROL SYSTEM

A. General description of the Control System

Based on the results in Section IV, it is possible to design a control system that implements the three optimization rules. The first and second optimization rules are easily implementable. This paper proposes a new implementation of the third rule based on (6) that can be written in the form:

$$\psi_m^{op} = \frac{2(r_s + r_r)}{\lambda_1^{op}} I_{rq}^{op} = k_{\psi I}(\omega_m) I_{rq}^{op}. \tag{21}$$

Since in region B λ_1^{op} is constant, (21) results in a linear $\psi_m^{op} - I_{rq}^{op}$ relationship in this region.

The airgap flux reference calculation (21) is implemented with two limiters to establish the minimum and maximum flux levels (Fig. 9). The low pass filter is used to avoid a high level of oscillations in the reference airgap flux. It also helps in the stabilization of the reference flux.

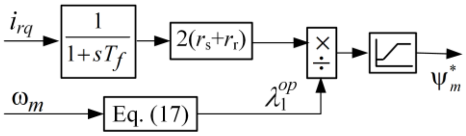

Fig. 9 Reference airgap flux calculator.

Fig. 10 illustrates a block diagram of the general control system. This control system can be implemented using two independent low-cost DSPs: one controlling the stator VSI and the other controlling the rotor VSI. An implementation on a single DSP is also possible.

The *current type* airgap flux estimator, needed for the implementation of flux orientation, is used in this case [26]. It computes the airgap flux in the flux reference frame using the stator and rotor current measurements and the rotor position measured by an encoder. The airgap orientation is enforced by controlling the *q*-axis flux component to zero (Fig. 10). This is done using two (d and q) direct flux controllers. The *dq* rotor currents are controlled by two PI controllers where the *d*-axis current reference comes from the optimal split condition and the *q*-axis component reference is determined via (7) using the torque reference and estimated airgap flux (Fig. 10).

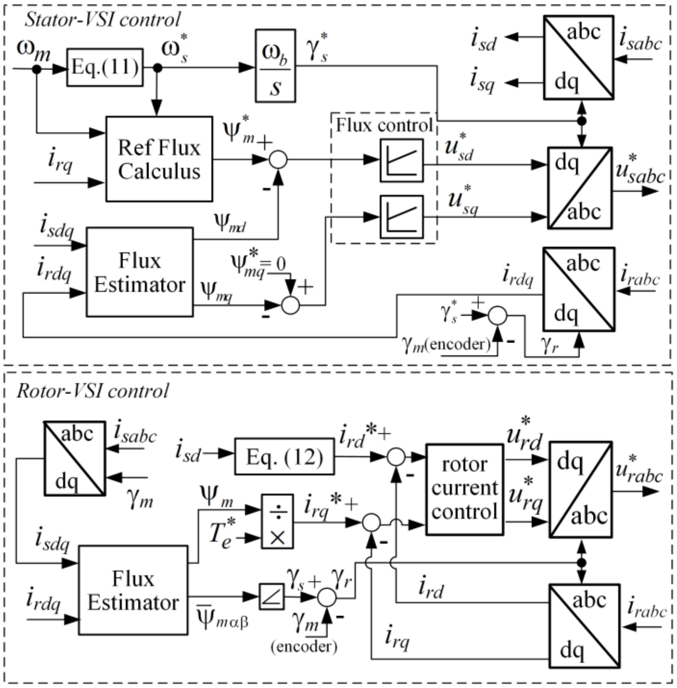

Fig. 10 Block diagram of the control system.

B.Simulation Results

As a preliminary validation, the response of the system is shown in Fig. 11 for two operating regions, B and C, as well as the transition between them due to a torque step. This figure was obtained through simulation in Matlab/Simulink.

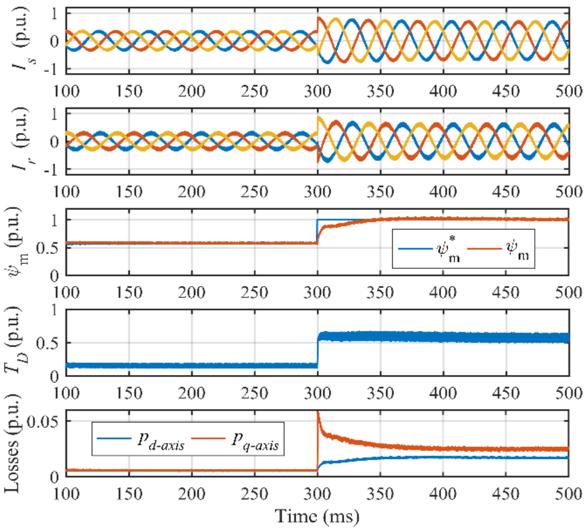

Fig. 11 Simulation results showing the system response to a step on the torque reference ($\omega_m = 1\,p.u.$).

The stator and rotor currents have almost the same frequency because the system is operating at a slip close to -1. In the first instants, region B, p_{d-axis} equals p_{q-axis} as predicted by (13). The airgap flux level is slightly higher than 0.5 p. u. After the torque step the flux hits the upper limit, then leading to a transition from region B to region C, with consequent violation of (13), leading to p_{q-axis} being higher than p_{d-axis}.

VI. SENSITIVITY ANALYSIS

The proposed control method is based on (21), which relates the optimal flux with I_{rq}^{op}. Any errors in this function will affect the reference flux, causing the operating point obtained to drift from the actual optimal operating condition.

Lagrange multiplier λ_1^{op} is the key variable to understand the sensitivity to parameters. To compute the reference flux for a torque T_D, (22) can be used:

$$\psi_m = \sqrt{\frac{2(r_s+r_r)}{\lambda_1}T_D}\,. \tag{22}$$

Given (17), (22) is affected by errors in r_s, r_r, L_m and in the function $f(\omega_s,\omega_m)\sim f(\omega_m)$, leading to errors in ψ_m.

Mismatches in ψ_m affect the total losses p_t through both *d*-axis losses and *q*-axis losses, as described by (12) - (14).

The influence of parameter mismatches is evaluated using the definition (23), with p_t computed considering mismatches and p_t^{op} computed without mismatches.

$$Error = \frac{p_t - p_t^{op}}{p_t^{op}} \times 100\% \tag{23}$$

The values obtained for $\omega_m = 1\,p.u.$ and $\omega_m = 2\,p.u.$ are presented in Table I for $T_D = 0.15\,p.u.$. In region B there is almost no variation of this error with torque T_D.

TABLE I
INFLUENCE OF PARAMETER MISMATCHES ON THE TOTAL POWER LOSSES ($T_D = 0.15\ p.u.$)

Mismatch	Error (%)	
	$\omega_m = 1\ p.u.$	$\omega_m = 2\ p.u.$
$f'_{\omega_m} = 0.8 f_{\omega_m}$	0.125	0.31
$f'_{\omega_m} = 1.2 f_{\omega_m}$	0.1	0.23
$L'_m = 0.8 L_m$	0.83	0.26
$L'_m = 1.2 L_m$	0.38	0.096
$r'_s = 0.8 r_s$	0.046	0.095
$r'_s = 1.2 r_s$	0.047	0.082
$r'_r = 0.8 r_r$	0.012	0.0475
$r'_r = 1.2 r_r$	0.016	0.045
$\lambda_1 \approx 2\sqrt{f(\omega_m)\,(r_s + r_r)}$	6.98	1.29

The errors obtained are extremely small. The same algorithm was used when λ_1 in (21) is calculated ignoring term $r_s r_r / L_m^2$ in (17). The errors that are presented in the last row are included to allow a comparison with the experimental validation presented in Section VII-C.

VII. EXPERIMENTAL RESULTS

To verify the theory presented in the previous sections, a laboratory test-rig was utilized, which includes a WRIM and two VSI inverters connected to a 200 V dc laboratory network. The different numbers of turns in the stator and rotor windings of the machine were equalized by connecting a transformer to the stator. The two VSIs are controlled independently by using low-cost Microchip fixed point dsPIC30F4011 microcontrollers. There is no communication between the microcontrollers, but they share the output of the system sensors, including an encoder with 4096 ppr.

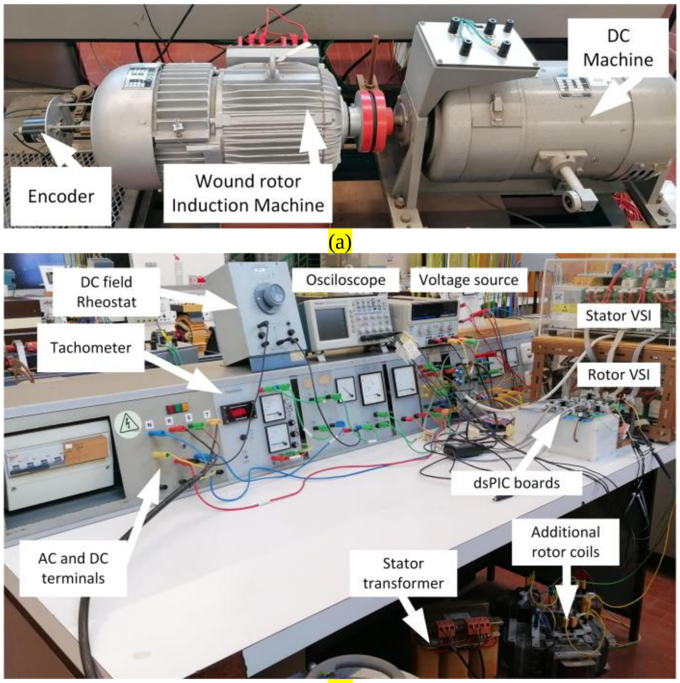

(a)

(b)

Fig. 12 Experimental setup: (a) electrical machines and encoder; (b) power electronics, measurement and control systems.

The real-time results are obtained from four PWM output channels per dsPIC, which are connected to low-pass RC filters. The WRIM is driven by a separate excitation dc motor, and the armature voltage adjusted by a simple three-phase variac and diode bridge. This setup causes slight variations in the rotor speed, depending on the load.

The differential anti-windup implementation was adopted for all PI controllers. The airgap flux controllers and rotor current controllers were designed using the ITAE criterion. A photograph of the experimental setup is shown in Fig. 12.

A. Open loop response

The open loop response to a decreasing ramp on the reference flux is shown in Fig. 13. The results in this figure were obtained using a first-order filter (τ=7 ms). The test was carried out at 1.0 p.u. rotor speed and 0.15 p.u. torque. Since this is a low power prototype, the losses in p.u., including semiconductor losses, are considerable. In both cases, the minimum total loss is obtained when p_{d-axis} intersects p_{q-axis}. These two variables are different in these two cases because semiconductor losses are considered in one case and omitted in the other one. Despite the significant semiconductor losses in this prototype, the optimal operating points are still close to each-other, with the airgap flux being slightly lower when semiconductor losses are not considered in the optimization procedure.

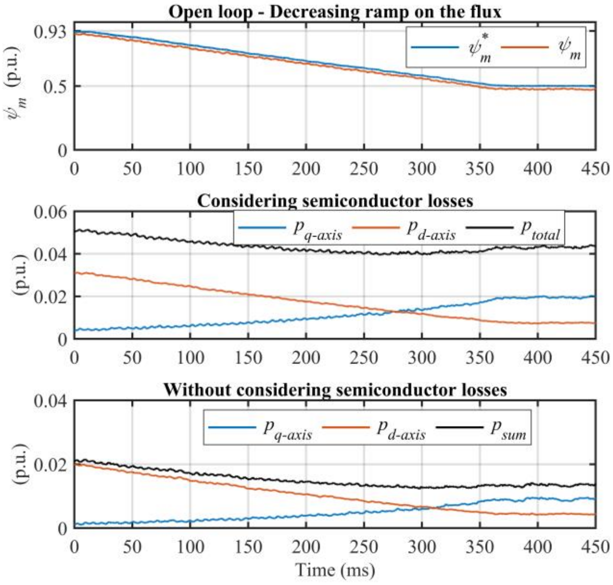

Fig. 13 Response to a decreasing ramp of the airgap flux in open loop.

Fig. 13 indicates that for and small-scale lab converter based on classic power electronics technology, semiconductor losses have some small influence on the optimal point. However, for new power electronics technology where semiconductor losses are much smaller, these losses can be ignored. It is important to note that the auxiliary functions p_{d-axis} and p_{q-axis} are mathematically different in these two cases.

As the optimal operation can be mathematically verified by comparing these two functions, they are shown in all experimental results presented in this section.

B. Response to a Step on the Reference Torque. Step to region B and step to region C.

Fig. 14 and Fig. 15 show the system responses to a step change in the reference torque, from zero to 0.2 p.u. and 0.6 p.u. respectively.

In the first case, since the final flux is between the lower and upper limits, the system operates in region B, resulting in identical *d*- and *q*-axis losses p_{q-axis} and p_{d-axis}, according to (13). In the second case (Fig. 15), when the torque step is applied, the flux reaches the upper limit constraints, moving the operating point to region C and making p_{q-axis} and p_{d-axis} different.

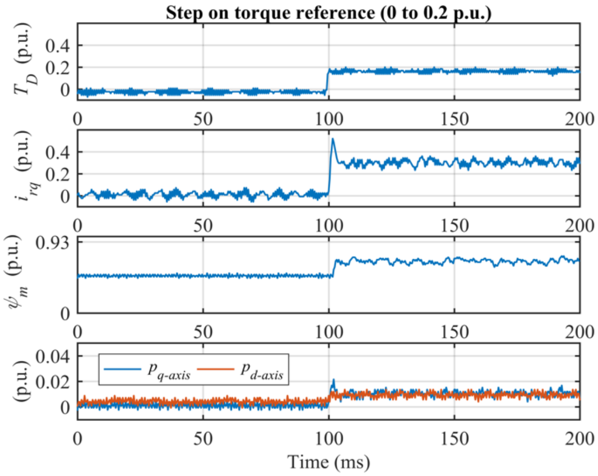

Fig. 14 Response to a 0.2 p.u. reference torque step at 1500 rpm.

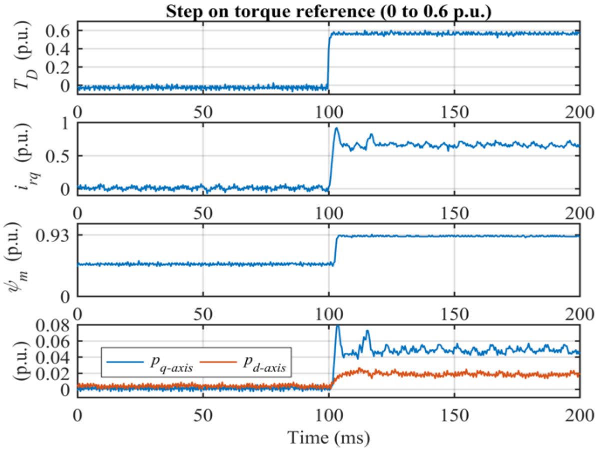

Fig. 15 Response to a 0.6 p.u. reference torque step at 1500 rpm.

The step response of the method presented in [19] under similar conditions as in Fig. 14 is illustrated in Fig. 16. In this case, the auxiliary functions p_{q-axis} and p_{d-axis} have different values compared with those in Fig. 14, as their definition in [19] involve extra terms.

Comparing Fig. 14 and Fig. 16 shows that that the method proposed here (see Fig. 14) has a slightly faster response. Although fast response is not a major benefit in this field of application (maximizing system efficiency), it highlights the advantage of avoiding the use of a PI controller and related tuning issues. The response time of the method in [19] depends on the PI parameters and on the operating point.

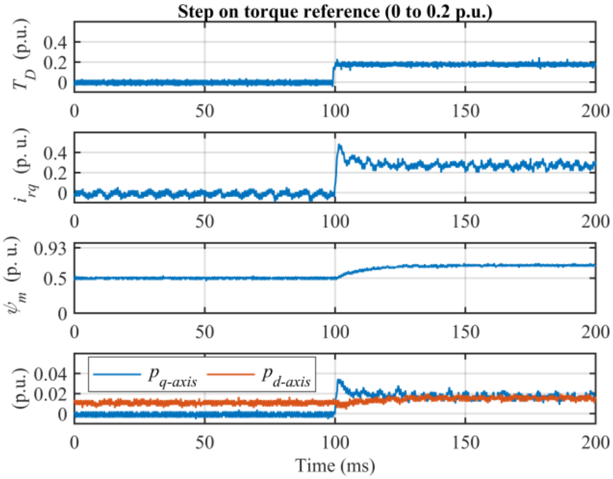

Fig. 16 Same result as Fig. 14 using the method in [19].

C. Response a Ramp in the Reference Torque

The response to a ramp in the reference torque is shown in Fig. 17 to Fig. 19 for different rotor speeds. The reference airgap flux starts from the minimum flux constraint value of 0.5 p.u.. At a certain torque level, the flux starts to increase, the system enters region B, and the λ_1^{op} parameter remains approximately constant as expected from (21) because it depends slightly on the rotor speed which changes slightly during the transient. The two types of losses p_{q-axis} and p_{d-axis} are also shown. They are equal when the system operates in region B. The evolution of the rotor current i_{rq}^{op} can be easily understood based on its dependency on the flux and torque.

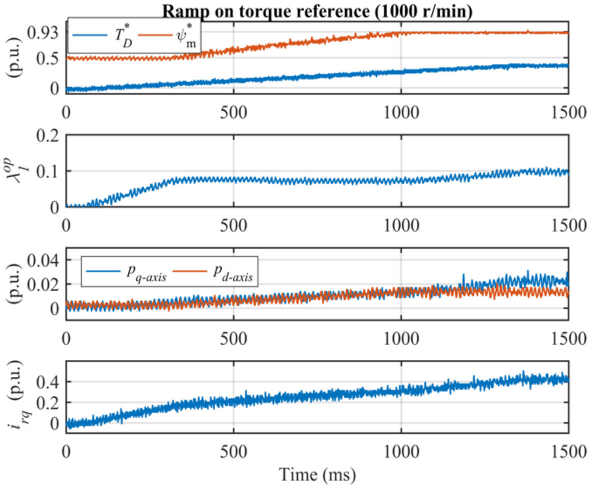

Fig. 17 Response to a ramp in the reference torque at 1000 rpm.

In Fig. 19 the flux reaches the upper constraint only at the end of the transient. This is the reason why both types of losses remain equal during the whole torque ramp.

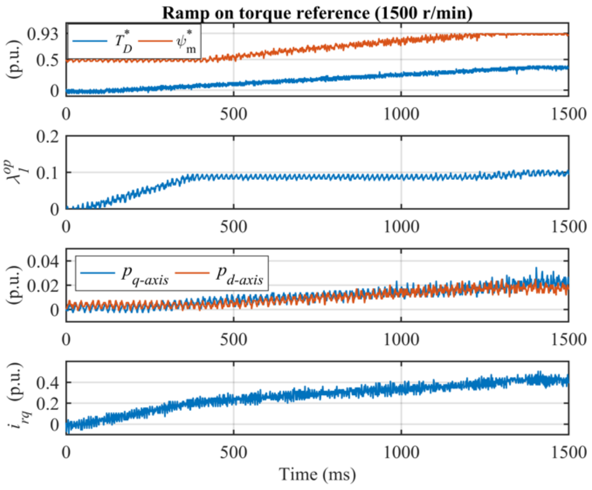

Fig. 18 Response to a ramp in the reference torque at 1500 rpm.

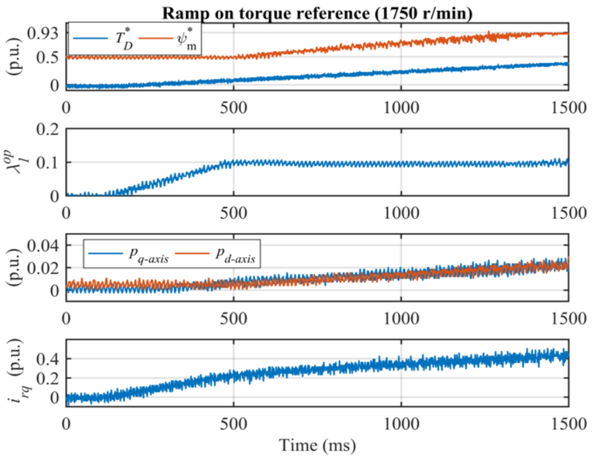

Fig. 19 Response to a ramp in the reference torque at 1750 rpm.

D. Response to a Reference Torque Ramp under Parameter Mismatches

The test in Fig. 18 was repeated when (22) is computed ignoring $r_s r_r / L_m^2$ in (17). The results are presented in Fig. 20.

The resulting error in λ_1^{op} is according to the sensitivity study. However, when compared with Fig. 18, no big differences appear: similar levels of p_t are obtained. The error in the losses is about 7%, i.e. approximately equal to the value computed in the last row in Table I.

I. CONCLUSION

This paper has presented a simplified control algorithm for minimizing the sum of core and Joule losses in a dual-VSI DFIG-dc system. The algorithm neglects semiconductor losses proportional to current magnitude, assuming the high performance of modern power electronics devices. Lagrange multipliers are used to optimize the system, leading to explicit expressions for optimal reference commands for inner magnetizing flux and rotor current controllers. The control system implements the optimal solution in an airgap field-oriented control framework.

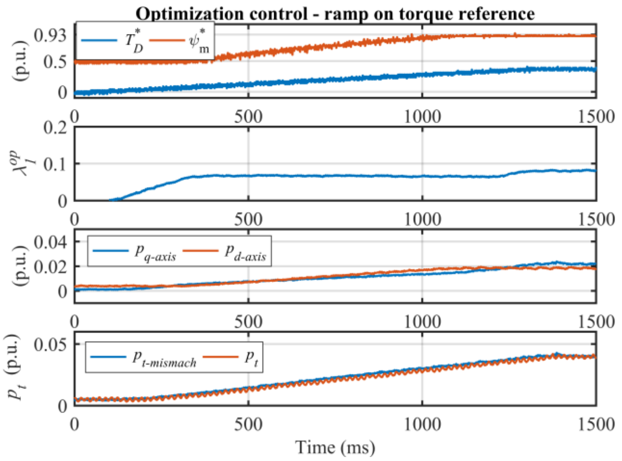

Fig. 20 Response to a ramp in the reference torque at 1500 rpm with mismatch in the parameters – i.e., ignoring the term $r_s r_r / L_m^2$ in (17) feeding into (20). A low-pass filter was used to mitigate oscillations.

As main novelties with respect to the existing literature, the proposed approach includes a new implementation for the airgap flux optimization that avoids handling implicit optimal conditions and related ancillary PI controllers for numeric inversion. A sensitivity analysis has revealed that the higher the speed, the lower the power loss drift from the optimal value caused by WRIM parameter mismatches. The experimental implementation was carried out using two independent low-cost DSPs. Simulation and experimental results have demonstrated the validity of the theoretical study presented.

APPENDIX I

Wound rotor induction machine ratings: 3.2 kW, 4-pole, 380/110 V, 8.1/19 A, delta-connected stator. Per-unit parameters use the following base values: S_B=5350 VA, f_B=50 Hz, U_B= 380 V, T_B=34 Nm.

TABLE II
SYSTEM AND CONTROL PARAMETERS

Parameters	
Resistances	r_s = 0.06 p. u., r_r = 0.05 p. u.
Inductances	L_m=1.5 p.u., L_{ks}=0.10 p.u., L_{kr}=0.10 p.u.
Core loss components	p_{se0} = 0.015 p.u, p_{sh0} = 0.007 p.u, p_{re0} = 0.013 p.u, p_{rh0} = 0.005 p.u
Inverter losses	p_{invs0} = 0.04 p.u., p_{invr0} = 0.04 p.u.
Turns ratio	$n_1/n_2 = 3.45$
Stator transformer	$S_n = 4kVA,\ 220\,V/110\,V$
Airgap flux limits	$\psi_{min} = 0.5\ p.u.,\ \psi_{max} = 0.93\ p.u.$
PI controller bandwidths	Rotor current =6 p.u. airgap flux=0.6 p.u.
VSI switching frequency	3 kHz
Sampling frequency	10 kHz
Output channel RC filter bandwidth	600 Hz to filter 30 kHz switching.

REFERENCES

[1] R. Cárdenas, R. Peña, S. Alepuz, G. Asher, “Overview of control systems for the operation of DFIGs in wind energy applications,” IEEE Trans. Ind. Electron., vol. 60, no. 7, pp. 2776–2798, July 2013.

[2] A. Petersson, “Analysis, modeling and control of doubly-fed induction generators for wind turbines,” Ph.D. dissertation, Dept. Energy Environ., Chalmers Univ. Technol., Gotemburg, Sweden, 2005.

[3] S. Yan, A. Zhang, H. Zhang and J. Wang, “Control scheme for DFIG converter system based on DC-transmission,” in *IET Electric Power Applications*, vol. 11, no. 8, pp. 1441-1448, 9 2017.

[4] H. Kakigano, Y. Miura, T. Ise "Low-voltage bipolar-type dc microgrid for super high-quality distribution,” IEEE Trans. Power Electron., vol. 25, no. 12, pp. 3066-3075, Dec. 2010.

[5] G. D. Marques, M. F. Iacchetti, “DFIG Topologies for DC Networks: a review on control and design features,” IEEE Trans. Pow. Electron., vol. 34, no. 2, pp. 1299-1316, Feb. 2019.

[6] H. Nian, X. Yi, “Coordinated control strategy for doubly-fed induction generator with dc connection topology,” IET Renew. Power Gener., vol. 9, no. 7, pp. 747–756, Aug. 2015.

[7] Y. Kawabata, E. Ejiogu and T. Kawabata, “Vector-controlled double-inverter-fed wound-rotor induction motor suitable for high-power drives,” *IEEE Trans. Ind. Appl.*, vol. 35, no. 5, pp. 1058-1066, Sep/Oct 1999.

[8] S. Yan, A. Zhang, H. Zhang, J.Wang, and B. Cai, “Optimized and coordinated model predictive control scheme for DFIGs with DC-based converter system,” J. Mod. Power Syst. Clean Energy, vol. 5, pp. 620–623, 2017.

[9] F. Bonnet Francois, P. E. Vidal and M. Pietrzak-David, “Dual direct torque control of doubly fed induction machine,” *IEEE Transactions on Industrial Electronics*, vol. 54, no. 5, pp. 2482-2490, Oct. 2007.

[10] M. Abdellatif, M. Debbou, I. Slama-Belkhodja, and M. Pietrzak-David, “Simple low-speed sensorless dual DTC for double fed induction machine drive,” IEEE Trans. on Ind. Electron., vol. 61, pp. 3915-3922, 2014.

[11] G. Poddar and V. T. Ranganathan, “Direct-torque and frequency control of double-inverter-fed slip-ring induction motor drive,” *IEEE Trans. Ind. Electron.*, vol. 51, no. 6, pp. 1329-1337, Dec. 2004.

[12] G. Poddar and V. T. Ranganathan, "Sensorless double-inverter-fed wound-rotor induction-machine drive," *IEEE Trans. Ind. Electron.*, vol. 53, no. 1, pp. 86-95, Feb. 2006.

[13] B. Rabelo, W. Hofmann, and L. Pinheiro, “Loss reduction methods for doubly-fed induction generator drives for wind turbines,” in Proc. Int. Symp. Power Electron., Elect. Drives, Autom. Motion, 2006,.

[14] Y. Han and J. I. Ha, “Control Method of Double Inverter Fed Wound Machine for Minimizing Copper Loss in Maximized Operating Area,” IEEE Trans. on Ind. Electron., vol. 64, no. 10, pp. 7700-7710, Oct. 2017.

[15] B. Zhang, W. Hu, and Z. Chen, “Loss minimizing operation of doubly fed induction generator based wind generation systems considering reactive power provision,” in Proc. 40th Annu. Conf. IEEE Ind. Electron. Soc., 2014, pp. 2146–2152.

[16] J. Gillet, M. P. David and F. Messine, “Optimization of the control of a doubly fed induction machine,” IEEE 11th Int. Work. Electron., Contr., Meas., Sign. & Appl.Mechatron., Toulouse, 2013, pp. 1-5.

[17] G. D. Marques, M. F. Iacchetti, “Field Weakening Control for Efficiency Optimization in a DFIG connected to a dc Link” IEEE Trans. Ind. Electron., Vol. 63, No.6, pp. 3409 – 3419, June. 2016.

[18] S. M. A. Cruz, G. D. Marques, P. F. C. Gonçalves and M. F. Iacchetti, "Predictive Torque and Rotor Flux Control of a DFIG-DC System for Torque Ripple Compensation and Loss Minimization," *IEEE Trans. on Ind. Electron*, vol. 65, no. 12, pp. 9301-9310, Dec. 2018.

[19] G. D. Marques, Sérgio M. A. Cruz, Matteo F. Iacchetti, “Minimum-Loss Control Strategy for a Dual-VSI DFIG DC System” IEEE Trans on Ind. Electron., vol.67, no. 10, pp 8175-8185, Oct. 2020.

[20] G. D. Marques, Matteo F. Iacchetti, Sérgio M. A. Cruz , “Stability Study of a Minimum-Loss Control Strategy for a Dual-VSI DFIG DC System” IEEE 14th International Conference on Compatibility, Power Electronics and Power Engineering (CPE-POWERENG), pp. 297-302, July. 2020.

[21] J. Millan, P. Godignon, X. Perpina, A. Perez-Tomas, and J. Rebollo, “A survey of wide bandgap power semiconductor devices,” *IEEE Transactions on Power Electronics*, vol. 29, no. 5, pp. 2155–2163, 2014

[22] Pedro B. C. Costa, J. Fernando Silva, S. F. Pinto, “Experimental Evaluation of SIC MOSFET and GaN HEMT losses in Inverter Operation” IECON 2019 45th Annual Conference of the IEEE Industrial Electronics Society, vol. 1 p6595-6600, Oct. 2019.

[23] W. Xu, R. y. Yu, Z. Guo and A. Q. Huang, “Design of 1500V/200kW 99.6% Efficiency Dual Active Bridge Converters Based on 1700V SiC Power MOSFET Module,” 2020 IEEE Energy Conversion Congress and Exposition (ECCE), 2020, pp. 6000-6007, doi: 10.1109/ECCE44975.2020.9235903.

[24] Z. Yuan et al., “A Three-phase 450 kVA SiC-MOSFET Based Inverter with High Efficiency and High-Power Density By Using 3L-TNPC,” 2021 IEEE Applied Power Electronics Conference and Exposition (APEC), 2021, pp. 2171-2176, doi: 10.1109/APEC42165.2021.9487253.

[25] E. Gurpinar and B. Ozpineci, “Loss Analysis and Mapping of a SiC MOSFET Based Segmented Two-Level Three-Phase Inverter for EV Traction Systems,” 2018 IEEE Transportation Electrification Conference and Expo (ITEC), 2018, pp. 1046-1053, doi: 10.1109/ITEC.2018.8450188.

[26] G. Abad, J. Lopez, M. Rodriguez, L. Marroyo, G. Iwanski, *Doubly Fed Induction Machine: Modeling and Control for Wind Energy Generation*, John Wiley & Sons, 2011, p508.